Towards Real-Time Simulation of Two-Dimensional Models for Electrodeposition/Stripping in Lithium-Metal Batteries

Taejin Jang[a], Lubhani Mishra[b], Krishna Shah[b], Akshay Subramaniam[c], Maitri Uppaluri[a], Scott A. Roberts[d], and Venkat R. Subramanian[a, b]

[a] Materials Science and Engineering Program, Texas Materials Institute, The University of Texas at Austin, Austin, TX 78712, USA
[b] Walker Department of Mechanical Engineering, Texas Materials Institute, The University of Texas at Austin, Austin, TX 78712, USA
[c] Department of Chemical Engineering, University of Washington, Seattle, WA 98195, USA
[d] Thermal/Fluid Component Sciences Department, Engineering Sciences Center, Sandia National Laboratories, Albuquerque, NM 87123, USA

In this study, a numerical modeling framework is developed to model and predict the morphological evolution in lithium metal batteries. A two-dimensional moving boundary model is used to simulate the dendritic growth from a nucleated lithium metal protrusion at the surface of the negative electrode. Depending on the geometric, kinetic, and transport parameters, the growth rate and shape of the lithium seed varies and in turn, affects the cyclability and capacity loss of the battery. Compared to conventional approaches, the proposed approach enables simulation of 100 cycles of charge-discharge in less than 1 minute. This robust model and algorithm for predicting metal deposition and stripping in lithium metal batteries brings together the mesoscale and electrochemical models and can pave the path towards specifically tailored dendrite-free morphological evolution to make lithium metal anodes viable in commercial systems.
.

Introduction

Lithium metal anode has been tipped to be the most likely successor of graphite anode in the next generation lithium-based batteries due to the possibility of achieving high redox potential and specific capacity. While lithium plating is the key to the high specific capacity, the surface morphology deteriorates over cycles due to evolution of dendrites and dead lithium (1-11). This results in capacity loss and is a safety risk due to the possibility of internal short-circuit caused by dendrites piercing through the separator. This hinders the translation towards commercialization of this potential technology as there is still a lack of understanding of the conditions that lead to such undesired interfacial phenomena (12-15).

In order to understand and minimize these impediments, it is crucial to have detailed physics-based 2D electrochemical models and ability to perform robust simulations. Recently, we have provided well-defined 2D models relevant for lithium metal battery and elucidated the significance of rigorous convergence analysis (16). Although there has

been remarkable progress in the experimental design of lithium metal batteries with improved performance, there is limited work on accurate models and robust simulation to study microstructure evolution in the lithium metal anode (17-23). There also lacks a modeling framework that relates morphological changes with corresponding system-level response in a simultaneous manner. Such a framework can prove to be useful in designing lithium metal batteries with long life and high performance. We have reviewed that the current literature fails to fulfill the gap between the electrochemical and mesoscale models. Electrochemical models typically ignore the mesoscale, moving boundaries, and pressure models while mesoscale models cannot predict electrochemical signatures (voltage-time curves) with enough precision. Thus, the present models being developed are designed to couple the microstructure evolution with voltage-time response to capture the lithium growth and understand the experimental signatures for the current and voltage curves at the lithium metal electrode. We have recently reported simple 1D models to study plating and stripping in lithium metal anode (24-25).

The lithium metal battery is a complex system with key phenomena occurring at different length and time scales, which affect the performance and life of the battery as shown in Fig. 1. Several approaches like level-set, phase-field, Arbitrary Lagrange-Eulerian (ALE), etc. are widely used to model the moving boundary in lithium metal batteries. We have analyzed the performance of the various numerical schemes for the Laplace equation which solves for the potential distribution within the liquid electrolyte in the absence of concentration gradients. Several validations were performed with the help of FEM based commercial solver, COMSOL Multiphysics for in-house codes based on different numerical schemes. In addition, a careful analysis of commonly used methods, ALE and phase-field method, to track the moving boundary highlighted some issues with the use of these approaches for the model of interest.

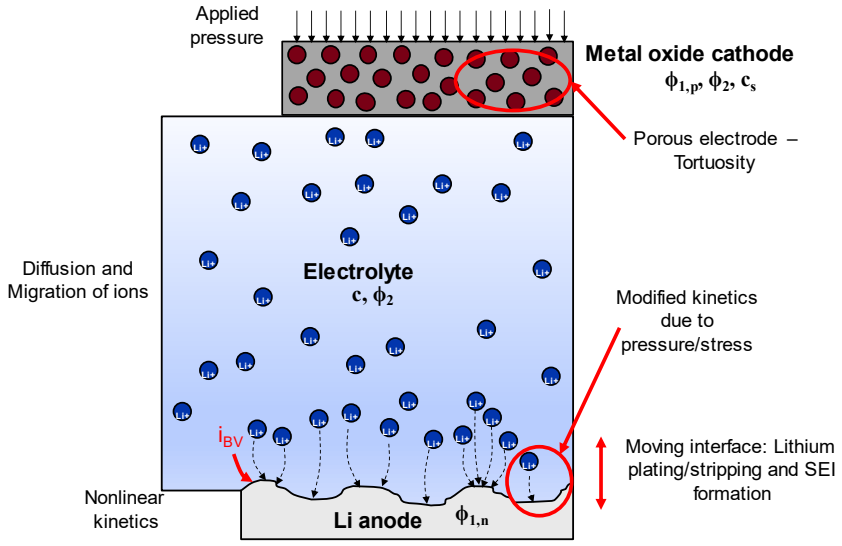

Figure 1. Key physical phenomena in lithium metal batteries

Our goal is to develop algorithms that help achieve desired grid resolution, handle singularities in the domain, account for discontinuous transport properties, and a significant improvement in the order of accuracy, memory footprint and simulation speed (10-100x faster) compared to the current state of the art simulation tools. The proposed hybrid numerical scheme can help in developing and implementing robust, convergent,

and efficient algorithms for the direct simulation of multiscale and coupled meso-scale and electrochemical engineering models. The algorithms developed based on the approach presented in this paper are able to predict up to 100 cycles of charge/discharge in less than 1 minute which may help enable model-based design, real-time control, and fast charging using model-based charging protocols. These improved algorithms, running in real-time, coupled with advanced models will lead us to tailored designs for fast charging and long-lasting lithium metal batteries, which can make this lithium battery technology viable in commercial systems.

Model Development

Figure 2 shows a simple geometry representing the separator within a lithium metal battery. The initial model comprises of a protrusion of lithium metal at the anode/electrolyte interface which mimics the non-uniform lithium deposition at the anode due to surface inhomogeneities. This seed deposit serves as a site for dendritic growth and has been modeled as a Gaussian curve with seed height as 1 μm at the lithium anode surface. The separator is filled with a binary liquid electrolyte with dimensions for length and thickness as L_x = 10 μm and L_y = 50 μm in x and y directions, respectively. The two-dimensional moving boundary model is developed and solved for the liquid phase potential and lithium ion concentration within the separator to simulate the electrodeposition/stripping of the lithium metal during the charge/discharge cycles of the battery.

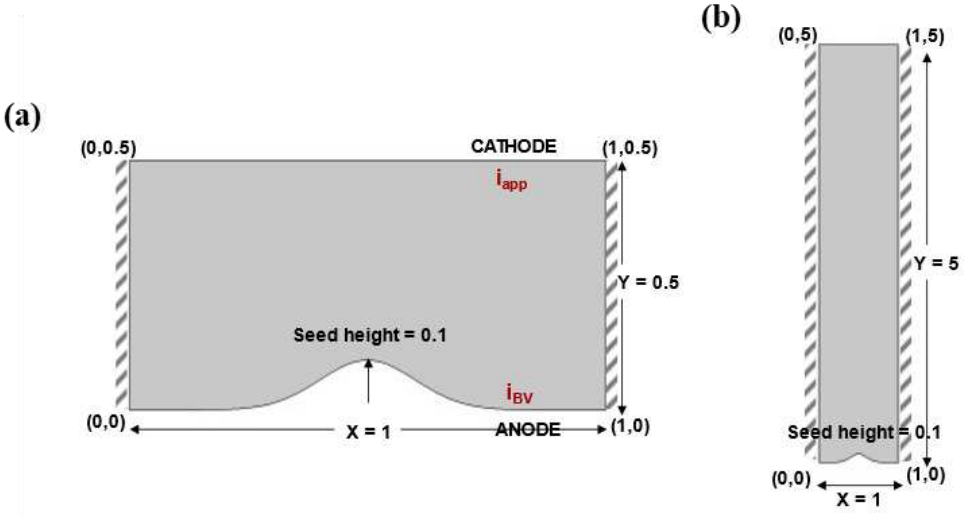

Figure 2. Schematic for the model for lithium metal deposition at the anode surface (a) initial geometry for validation and (b) actual geometry for simulations (The dimensions are shown in scaled form).

Further, the porosity of the separator is neglected, and the electrolyte shares the whole domain. The governing equations and boundary conditions in the model are solved with the modified Butler-Volmer kinetics at the anode-electrolyte interface which is simulated as a moving boundary to capture the 2D growth due to lithium deposition at the anode. A uniform current density is assumed at the other end of the separator at $y = L_y$. The cathode side kinetics are not considered in this model. The left and right boundaries of

the domain are assumed to be insulated and modeled using a zero flux boundary condition, making the computation domain considered in this study to be a repeating unit.

We have developed and tested a robust numerical framework to study the two-dimensional nature of the growth/deposition at the bottom with charge/discharge cycles while accounting for the kinetics at the anode. The model has been studied to delineate the effects of design, transport, and kinetic parameters, *viz*., the aspect ratio of the separator domain, height, and shape of the deposited seed, diffusivity, and conductivity of the liquid electrolyte, applied and exchange current densities, transference number, etc.

For a binary electrolyte, the flux density of each dissolved species in terms of diffusion, migration and convection is given by (26):

$$N_i = -D_i \nabla c_i - z_i u_i F c_i \nabla \phi_i + c_i v \ , i = 1,\ 2 \qquad [1]$$

The ionic current in an electrolytic solution is due to the motion of charged species and can be expressed as:

$$i = -F \sum_i z_i N_i \ , i = 1,\ 2 \qquad [2]$$

The electroneutrality assumption gives:

$$\sum_i z_i c_i = 0 \ , \ i = 1,\ 2 \qquad [3]$$

Substituting, Eq. [1] in Eq. [2], the expression for the current density in the solution in terms of species fluxes can be given as:

$$i = F \sum_i z_i D_i \nabla c_i + F^2 \nabla \phi \sum_i z_i^{\,2} u_i c_i - Fv \sum_i z_i c_i \qquad [4]$$

By virtue of Eq. [3] for electroneutrality, the last term in Eq. [4] is zero.

$$i = F \sum_i z_i D_i \nabla c_i + F^2 \nabla \phi \sum_i z_i^{\,2} u_i c_i \qquad [5]$$

The further development of the model equations is branched into two models where (a) Model 1 denotes the case when there are no concentration gradients in the solution and (b) Model 2 includes the effects of variations in electrolyte composition, i.e., concentration gradients are accounted for in the separator domain.

Model 1

In the absence of concentration gradients in the solution, Eq. [5] reduces to the common concept of electrolytic conductance:

$$i = F\sum_i z_i D_i \cancel{\nabla c_i} + F^2 \nabla\phi \sum_i z_i^2 u_i c_i \quad , i = 1, 2 \qquad [6]$$

$$i = -\kappa \nabla\phi \qquad \text{where} \quad \kappa = -F^2 \sum_i z_i^2 u_i c_i \qquad [7]$$

Equation [7] is an expression for Ohm's law valid for electrolytes in the absence of concentration gradients. In view of the assumption of electroneutrality, the conservation of charge reduces to the following equation:

$$\nabla \cdot i = 0 \qquad [8]$$

Insertion of Eq. [7] into Eq. [8] yields

$$\nabla \cdot \left(-\kappa \nabla\phi \right) = 0 \quad \Rightarrow \quad \nabla^2 \phi = 0$$
$$\Rightarrow \quad \frac{\partial^2 \phi}{\partial x^2} + \frac{\partial^2 \phi}{\partial y^2} = 0 \qquad [9]$$

Thus, the potential satisfies the Laplace equation in a region with uniform concentration of the cations and anions. From Eq. [7], the boundary conditions in the separator domain for the electrolyte potential for Model 1 are given below following the assumption of equal diffusivities for the ions (i.e., $D_1 = D_2 = D$) and substituting the relationship provided by Nernst-Einstein equation for diffusivity ($D_i = RTu_i$) :

$$\frac{\partial \phi}{\partial x} = 0 \quad at \quad x = 0,\ L_x \qquad [10]$$

$$\frac{\partial \phi}{\partial y} = \frac{i_{app,1C} CrateRT}{2c_0 DF^2} \quad at \quad y = L_y \qquad [11]$$

$$n \cdot \nabla\phi = \frac{\partial \phi}{\partial x} n_x + \frac{\partial \phi}{\partial y} n_y = \frac{i_{BV} RT}{2c_0 DF^2} \quad at \quad y = s(x,t) \qquad [12]$$

The velocity of the moving boundary at the bottom interface is prescribed by the Faraday's law as (6):

$$\frac{\partial s}{\partial t} = \frac{M_w}{\rho} \frac{i_{BV}}{F} \qquad [13]$$

The kinetics at the electrode-electrolyte interface is governed by the modified Butler Volmer kinetics as given below where the equilibrium potential difference is considered to be zero in the expression for activation overpotential for simplification and the reference electrode potential is set as zero.

$$i_{BV} = -i_0 \frac{\eta F}{RT}, \quad \eta = 0 - \phi \qquad [14]$$

Model 1: Non-dimensionalization

Table I lists the scaling variables used for non-dimensionalization of Model 1. The scaled model 1 along with the boundary and initial conditions and equation for moving boundary velocity takes the following form:

Table I. Scaling variables and dimensionless groups used in the models.

Scaling variables	
x'	$= x/L_x$
y'	$= y/L_x$
c'	$= c/c_0$
ϕ'	$= \phi/\phi_0$
s'	$= s/L_x$
τ	$= t/\left(3600/\lvert Crate\rvert\right)$
Dimensionless Groups	
δ	$= \frac{\left(i_{app,1C} L_x Crate\right)}{\left(2FDc_0\right)}$
Da	$= \frac{i_0 L_x}{2DFc_0}$
Pe	$= \frac{M_W i_0}{\rho F} \frac{L_x}{D}$
ϕ_0	$= \frac{RT}{F}$
τ_D	$= \frac{\left(Crate L_x^{\,2}\right)}{\left(3600D\right)}$
H	$= \frac{L_y}{L_x}$

$$\frac{\partial^2 \phi'}{\partial x'^2} + \frac{\partial^2 \phi'}{\partial y'^2} = 0 \qquad [15]$$

$$\frac{\partial \phi'}{\partial x'} = 0 \quad at \quad x' = 0\ ,\ 1 \qquad [16]$$

$$\frac{\partial \phi'}{\partial y'} = \frac{i_{app,1C} L_x Crate}{2c_0 DF} = \delta \quad at \quad y' = H \qquad [17]$$

$$\frac{\partial \phi'}{\partial x'} n_x' + \frac{\partial \phi'}{\partial y'} n_y' = -\frac{i_0 L_x \left(0 - \phi'\right)}{2 c_0 D F} = -Da \cdot \left(0 - \phi'\right) \quad at \quad y' = s'(x', t) \tag{18}$$

$$\begin{aligned} \frac{\partial s'}{\partial \tau} &= -\frac{M_w}{\rho} \frac{i_0}{F} \frac{3600}{L_x \left| Crate \right|} \left(0 - \phi'\right) = -\frac{M_w}{\rho} \frac{i_0}{F} \frac{3600}{L_x \left| Crate \right|} \left(0 - \phi'\right) \frac{L_x D}{L_x D} \\ &= -\left(\frac{M_w}{\rho} \frac{i_0}{F} \frac{L_x}{D} \right) \cdot \left(\frac{3600}{\left| Crate \right|} \frac{D}{{L_x}^2} \right) \left(0 - \phi'\right) \\ &= -\frac{Pe}{\tau_D} \left(0 - \phi'\right) \end{aligned} \tag{19}$$

$$s'(x', 0) = 0.1 e^{-50(x' - 0.5)^2} \quad at \ \tau = 0 \tag{20}$$

Model 1: Freeze Domain Approach and Coordinate Transformation

The model assumes a Gaussian curve for the morphology of the lithium metal electrode, but the domain constantly evolves as the reaction proceeds during both deposition and stripping of the lithium metal. Conventional discretization methods like finite difference or finite volume require re-meshing of the domain at every time step with non-uniform grid distribution based on the two-dimensional evolution of the lithium metal surface. This procedure is computationally expensive in terms of speed and memory usage. In this work, the surface morphology of the lithium-metal anode is expressed using a morphology function $s(x,t)$. However, the introduction of a new variable alone does not improve the complexity of this two-dimensional model as the moving interface evolves in both x- and y- directions with time deforming the entire domain. In order to freeze the deforming domain, we introduce the coordinate transformation of y-axis as (27):

$$y' = s'\left(X, \tau\right) + Y\left(1 - s'\left(X, \tau\right) / H\right) \tag{21}$$

The transformed X and Y axes are still perpendicular, but the scale is different especially in Y. While the original domain varied from $s'(x',\tau)$ to H in scaled coordinates, the transformed domain ranges from 0 to H in y-dimension along the entire x-dimension. Thus, this transformation results in a square geometry, regardless of the geometry of the initial lithium seed and morphology evolution (Fig. 3). The notations for the pertinent variables (x', y', s' and ϕ) under the transformed coordinate system are given as X, Y, S and Φ, respectively. Since the scalars are not affected by the directions, the X and Y components of the normal flux are given as:

$$n_X = -\frac{\partial S}{\partial X} \Bigg/ \sqrt{1 + \left(\frac{\partial S}{\partial X} \right)^2} \tag{22}$$

$$n_Y = 1 \Bigg/ \sqrt{1 + \left(\frac{\partial S}{\partial X} \right)^2} \tag{23}$$

The transformed model equations can be summarized as follows:

$$\frac{\partial^2\Phi}{\partial X^2}+\left\{\frac{1+(1-Y)^2}{(1-S)^2}\left(\frac{\partial S}{\partial X}\right)^2\right\}\frac{\partial^2\Phi}{\partial Y^2}-2\frac{1-Y}{1-S}\frac{\partial S}{\partial X}\frac{\partial^2\Phi}{\partial X\partial Y} -\frac{1-Y}{1-S}\frac{\partial^2 S}{\partial X^2}\frac{\partial\Phi}{\partial Y}-2\frac{1-Y}{(1-S)^2}\left(\frac{\partial S}{\partial X}\right)^2=0 \quad [24]$$

$$\frac{\partial\Phi}{\partial Y}=\delta(1-S) \quad at \quad Y=H \quad [25]$$

$$-\frac{\partial S}{\partial X}\frac{\partial\Phi}{\partial X}+\left[\left(\frac{1-Y}{1-S}\right)\left(\frac{\partial S}{\partial X}\right)^2+\frac{1}{1-S}\right]\frac{\partial\Phi}{\partial Y}=Da\cdot\Phi\sqrt{1+\left(\frac{\partial S}{\partial X}\right)^2} \quad at \quad Y=0 \quad [26]$$

$$\frac{\partial\Phi}{\partial X}=0 \quad at \quad X=0\,,1 \quad [27]$$

$$\frac{\partial S}{\partial\tau}=\frac{Pe}{\tau_D}\cdot\Phi \quad [28]$$

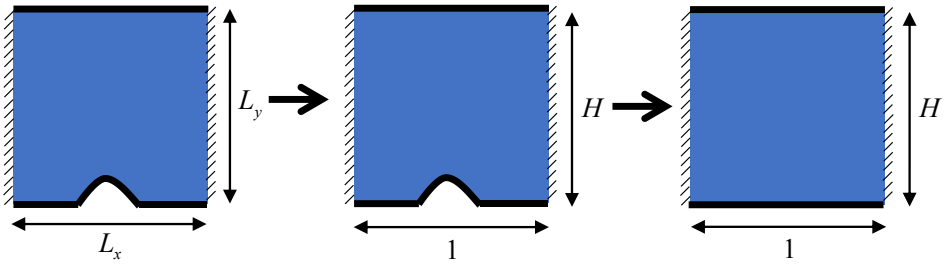

Figure 3. Transformation of the geometry and coordinate systems

Model 1: Spatial Discretization

In this paper, the governing equations and boundary conditions are discretized in space with a hybrid approach – a combination of finite volume and orthogonal collocation method. Since the original domain includes a moving boundary (Gaussian curve), application of collocation in the *x*-direction is not useful. Because of the moving boundary (in particular for domains with singularity at *y*=0), higher order methods in *x* reduce to only first order accuracy in *x* due to the Godunov limit (28). However, away from the moving boundary, the profiles are nearly smooth and hence collocation in the *Y* direction works very well for the geometry studied. Doing finite volume in both *X* and *Y* is possible, but it is found to be less efficient compared to the proposed approach. In addition, the model equations are not purely elliptic in the transformed coordinate (in particular, the collocation approach in the *X*-direction worsens the condition number for the linear algebra).

Therefore, we applied the cell-centered finite difference discretization along the *x*-dimension while the *y*-dimension is discretized with the orthogonal collocation method.

The number of node points considered in x-dimension are N, i.e., the step size h is $1/N$ in the scaled and transformed equations. The set of the model equations after the spatial discretization using the 2nd order finite difference method is given below:

$$\left(\frac{\Phi_{i-1}-2\Phi_i+\Phi_{i+1}}{2h^2}\right)+\left\{\frac{1+(1-Y)^2}{(1-S_i)^2}\left(\frac{S_{i+1}-S_{i-1}}{2h}\right)^2\right\}\frac{\partial^2\Phi_i}{\partial Y^2} - 2\frac{1-Y}{1-S_i}\left(\frac{S_{i+1}-S_{i-1}}{2h}\right)\frac{1}{2h}\left(\frac{\partial\Phi_{i+1}}{\partial Y}-\frac{\partial\Phi_{i-1}}{\partial Y}\right) - \frac{1-Y}{1-S_i}\left(\frac{S_{i-1}-2S_i+S_{i+1}}{2h^2}\right)\frac{\partial\Phi_i}{\partial Y}-2\frac{1-Y}{(1-S_i)^2}\left(\frac{S_{i+1}-S_{i-1}}{2h}\right)^2=0 \quad [29]$$

$$\frac{\partial\Phi_i}{\partial Y}=\delta\cdot(1-S_i) \quad at \quad Y=1 \quad [30]$$

$$-\left(\frac{S_{i+1}-S_{i-1}}{2h}\right)\left(\frac{\Phi_{i+1}-\Phi_{i-1}}{2h}\right)+\left[\left(\frac{1-Y}{1-S_i}\right)\left(\frac{S_{i+1}-S_{i-1}}{2h}\right)^2+1\right]\frac{\partial\Phi_i}{\partial Y} = Da\cdot\Phi_i\sqrt{1+\left(\frac{S_{i+1}-S_{i-1}}{2h}\right)^2} \quad at \;\; Y=0 \quad [31]$$

$$\frac{\Phi_1-\Phi_0}{h}=0 \quad at \quad X=0 \quad [32]$$

$$\frac{\Phi_{N+1}-\Phi_N}{h}=0 \quad at \quad X=1 \quad [33]$$

$$\frac{\partial S_i}{\partial\tau}=\frac{Pe}{\tau_D}\cdot\Phi_i(0) \quad [34]$$

It should be noted that S_i is only a function of X and τ while Φ_i is a function of both X and Y and τ. Thus, when we apply the orthogonal collocation method for discretization in Y direction with only one point, it is located at $Y = 0.5$ and is expressed as a Lagrange polynomial given by Eq. [35] at internal node points for $\Phi_{i,j}$. In the general form, it can be written for a series of orthogonal collocation points as expressed in Eq. [36] corresponding to M collocation points in the Y dimension.

$$\Phi_i(Y)=\Phi_{i,0}\frac{(Y-0.5)(Y-1)}{(0-0.5)(0-1)}+\Phi_{i,1}\frac{(Y-0)(Y-1)}{(0.5-0)(0.5-1)}+\Phi_{i,2}\frac{(Y-0)(Y-0.5)}{(1-0)(1-0.5)} \quad [35]$$

$$\Phi_i(Y)=\sum_{m=1}^{M}\left(\Phi_{i,m}\cdot\prod_{\substack{j=1\\ j\neq m}}^{M}\frac{Y-Y_j}{Y_m-Y_j}\right) \quad [36]$$

Model 1: Time Integration and Initialization

After the spatial discretization, the dependent variable Φ translates to an algebraic variable $\Phi_{i,j}(\tau)$ which is a function of τ and the values for *i* and *j* range from 0 to *N* and *M*, respectively. Further, $S_i(\tau)$ is an ordinary differential equation (ODE) variable in the equation for the moving boundary velocity. The transient solution for the ODE equation would require an appropriate time step size, *dt*, to capture the gradients at the moving interface accurately as given by Eq. [37] (Euler-forward method). Also, the initial value at $\tau = 0$ is given by the Gaussian curve for the initial seed geometry at the lithium metal anode as defined in Eq. [38].

$$S_i(\tau + dt) = S_i(\tau) + dt \cdot \frac{Pe}{\tau_D} \cdot \Phi_{i,0}(\tau) \quad [37]$$

$$S_i(0) = 0.1e^{-50\left((i-1/2)h-0.5\right)^2} \quad [38]$$

For the two-dimensional growth at the moving interface, the direction of the moving boundary velocity is normal to the moving surface depicted by $S(X,\tau)$. In order to trace the moving boundary in this case, the normal at the moving surface needs to be resolved in *X* and *Y* components of the transformed coordinate system used in the freeze domain approach. The resolved *X* and *Y* components of the moving boundary $mb_i(Sx_i, Sy_i)$ are written as:

$$\begin{aligned} Sx_i(\tau + dt) &= Sx_i(\tau) + dt \cdot \frac{Pe}{\tau_D} \cdot \Phi_{i,0}(\tau) \cdot n_x \\ &= Sx_i(\tau) - dt \cdot \frac{Pe}{\tau_D} \cdot \Phi_{i,0}(\tau) \left(\frac{\partial S}{\partial X} \Big/ \sqrt{1 + \left(\frac{\partial S}{\partial X} \right)^2} \right) \end{aligned} \quad [39]$$

$$\begin{aligned} Sy_i(\tau + dt) &= Sy_i(\tau) + dt \cdot \frac{Pe}{\tau_D} \cdot \Phi_{i,0}(\tau) \cdot n_y \\ &= Sy_i(\tau) + dt \cdot \frac{Pe}{\tau_D} \cdot \Phi_{i,0}(\tau) \left(1 \Big/ \sqrt{1 + \left(\frac{\partial S}{\partial X} \right)^2} \right) \end{aligned} \quad [40]$$

$$\frac{\partial S_i}{\partial X} = \frac{S_{i+1} - S_{i-1}}{2h} + O\left(h^2\right) \quad [41]$$

A challenging part in this numerical scheme is to model the evolution of the moving boundary in a two-dimensional domain as the *X* coordinate shifts at each time step. Since the moving surface $S(X,\tau)$ is the function of *X* and τ, the evolution in the *y*-direction does not affect the reformulated geometry. However, the changes in the *x*-direction cause the shift of the node points along the *x*-axis and affect the distribution of the grid size in the finite difference scheme. In the present case, the node points shift away from the center towards right and left boundaries of the domain as shown in Fig. 4 and cause the scarcity of the grid points at the center of the seed. To resolve this issue, we reinitialize the node

points at the moving boundary as per the original grid size in the x-direction at every time step using spline interpolation. With the help of this interpolation, the moving boundary coordinates $mb_i(Sx_i, Sy_i)$ given by Eqs. [39-40] are reinitialized as $MB_i(SX_i, SY_i)$ which retain the grid step size in X and enable us to maintain the accuracy for the solutions of Φ at every time step. Fixing the location of node points in X enable second order accuracy in X as opposed to variable grid in X.

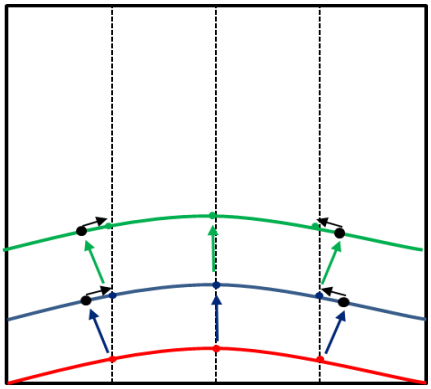

Figure 4. The evolution and initialization of moving boundary during time integration

Model 2

In this section, we will advance the development of Model 1 and relax the assumption of the constant electrolyte concentration within the separator to include the effects of the concentration variation in the liquid electrolyte. For a binary electrolyte, the flux density in x and y directions of each dissolved species in terms of diffusion and migration can be written as:

$$N_{1,x} = -D_1\left(\frac{\partial c_1}{\partial x}\right) - z_1 u_1 F c_1\left(\frac{\partial \phi}{\partial x}\right), \quad N_{1,y} = -D_1\left(\frac{\partial c_1}{\partial y}\right) - z_1 u_1 F c_1\left(\frac{\partial \phi}{\partial y}\right) \qquad [42]$$

$$N_{2,x} = -D_2\left(\frac{\partial c_2}{\partial x}\right) - z_2 u_2 F c_2\left(\frac{\partial \phi}{\partial x}\right), \quad N_{2,y} = -D_2\left(\frac{\partial c_2}{\partial y}\right) - z_2 u_2 F c_2\left(\frac{\partial \phi}{\partial y}\right) \qquad [43]$$

The material balance of the ionic species can be written using the Nernst-Planck equation in one dimension as:

$$\frac{\partial c_1}{\partial t} = -\left(\frac{\partial N_{1,x}}{\partial x} + \frac{\partial N_{1,y}}{\partial y}\right) \qquad [44]$$

$$\frac{\partial c_2}{\partial t} = -\left(\frac{\partial N_{2,x}}{\partial x} + \frac{\partial N_{2,y}}{\partial y}\right) \qquad [45]$$

For the Li-ion battery, the charge on the ions, i.e., z_1 and z_2 are +1 and -1, respectively. Further, substituting Eqs. [42-43] in Eqs. [44-45] and using the relationship provided by Nernst-Einstein equation for diffusivity ($D_i = RTu_i$), we get:

$$\frac{\partial c_1}{\partial t} = -\left[\begin{array}{l} \dfrac{\partial}{\partial x}\left(-D_1\left(\dfrac{\partial c_1}{\partial x}\right) - z_1 u_1 F c_1\left(\dfrac{\partial \phi}{\partial x}\right)\right) \\ + \dfrac{\partial}{\partial y}\left(-D_1\left(\dfrac{\partial c_1}{\partial y}\right) - z_1 u_1 F c_1\left(\dfrac{\partial \phi}{\partial y}\right)\right) \end{array}\right] \quad [46]$$

$$\frac{\partial c_2}{\partial t} = -\left[\begin{array}{l} \dfrac{\partial}{\partial x}\left(-D_2\left(\dfrac{\partial c_2}{\partial x}\right) - z_2 u_2 F c_2\left(\dfrac{\partial \phi}{\partial x}\right)\right) \\ + \dfrac{\partial}{\partial y}\left(-D_2\left(\dfrac{\partial c_2}{\partial x}\right) - z_2 u_2 F c_2\left(\dfrac{\partial \phi}{\partial x}\right)\right) \end{array}\right] \quad [47]$$

With the assumption for electroneutrality ($c_1 = c_2 = c$), we get the following coupled set of equations for the electrolyte concentration and potential:

$$\frac{\partial c}{\partial t} = -D_1\left[\frac{\partial}{\partial x}\left(-\frac{\partial c}{\partial x} - \frac{F}{RT}c\frac{\partial \phi}{\partial x}\right) + \frac{\partial}{\partial y}\left(-\frac{\partial c}{\partial y} - \frac{F}{RT}c\frac{\partial \phi}{\partial y}\right)\right] \quad [48]$$

$$\frac{\partial c}{\partial t} = -D_2\left[\frac{\partial}{\partial x}\left(-\frac{\partial c}{\partial x} + \frac{F}{RT}c\frac{\partial \phi}{\partial x}\right) + \frac{\partial}{\partial y}\left(-\frac{\partial c}{\partial y} + \frac{F}{RT}c\frac{\partial \phi}{\partial y}\right)\right] \quad [49]$$

On further mathematical simplification of these equations and assuming $D_1 = D_2 = D$, we arrive at the following decoupled equations for the concentration and potential within the electrolyte:

$$\frac{\partial c}{\partial t} = -D\left[\frac{\partial}{\partial x}\left(-\frac{\partial c}{\partial x}\right) + \frac{\partial}{\partial y}\left(-\frac{\partial c}{\partial y}\right)\right] = D\left(\frac{\partial^2 c}{\partial x^2} + \frac{\partial^2 c}{\partial y^2}\right) \quad [50]$$

$$0 = \frac{\partial}{\partial x}\left(c\frac{\partial \phi}{\partial x}\right) + \frac{\partial}{\partial y}\left(c\frac{\partial \phi}{\partial y}\right) \quad [51]$$

The ionic current in an electrolytic solution is due to the motion of charged species and can be expressed as given in Eq. [2]:

$$\begin{aligned} i &= F\sum_i z_i N_i, i = 1, 2 \\ \Rightarrow i &= F\left(N_1 - N_2\right) \end{aligned} \quad [52]$$

At the electrode-electrolyte interfaces, the anion flux is zero, i.e., $N_2 = 0$, the boundary conditions can be interpreted in the following form:

At $y = s(x,t)$ and L_y,

$$\left.\begin{array}{l} N_1 = -\dfrac{i}{F} \\ N_2 = 0 \end{array}\right] \Rightarrow \left.\begin{array}{l} -D\dfrac{\partial c}{\partial y} - \dfrac{DF}{RT} c \dfrac{\partial \phi}{\partial y} = -\dfrac{i}{F} \\ -D\dfrac{\partial c}{\partial y} + \dfrac{DF}{RT} c \dfrac{\partial \phi}{\partial y} = 0 \end{array}\right] \quad [53]$$

$$\Rightarrow \frac{\partial c}{\partial y} = \frac{i}{2FD} \;,\; c\frac{\partial \phi}{\partial y} = \frac{i}{2FD}\left(\frac{RT}{F}\right)$$

Now, the kinetics at the anode-electrolyte interface is governed by the modified Butler Volmer kinetics as follows similar to Eq. [12] where the equilibrium potential difference is considered to be zero in the expression for activation overpotential for simplification and the reference electrode potential is set as zero. A uniform current density, i_{app}, is applied at the cathode-electrolyte interface and the velocity of the moving boundary at the anode is given by Eq. [13].

$$i_{BV} = -i_0 \left(\frac{c}{c_0}\right)^{0.5} \frac{\eta F}{RT}, \quad \eta = 0 - \phi \quad [54]$$

Taking into account the mass conservation at the moving interface (29), the boundary conditions for Eqs. [50-51] take the following final form:

$$At\, x = 0\, and\, L_x, \;\; \frac{\partial c}{\partial x} = 0, \quad c\frac{\partial \phi}{\partial x} = 0 \quad [55]$$

$$At\, y = s(x,t), \;\; \frac{\partial c}{\partial x} n_x + \frac{\partial c}{\partial y} n_y = \frac{i_{BV}}{2FD} - \frac{c v_n}{D}$$
$$c\frac{\partial \phi}{\partial x} n_x + c\frac{\partial \phi}{\partial y} n_y = \frac{i_{BV}}{2FD}\left(\frac{RT}{F}\right) \quad [56]$$

$$At\, y = L_y, \;\; \frac{\partial c}{\partial y} = \frac{i_{app,1C} Crate}{2FD}$$
$$c\frac{\partial \phi}{\partial y} = \frac{i_{app,1C} Crate}{2FD}\left(\frac{RT}{F}\right) \quad [57]$$

The initial conditions for the system of equations is given as $c(x,y,0) = c_0$ and $s(x,0) = (1e-6)e^{-50(x-0.5e-6)^2}$.

It should be noted that the boundary condition at the moving boundary at $y = 0$ accounts for the interface transport. In order to maintain the mass conservation in the

domain with a moving boundary, the additional flux term is added which compensates for the diffusant disappearing from the domain.

Model 2: Non-dimensionalization

Using the scaling variables defined in Table I, the scaled equations along with the boundary and initial conditions and moving boundary velocity are listed below:

$$\frac{\partial c'}{\partial \tau} = \frac{3600D}{|Crate|L_x{}^2}\left(\frac{\partial^2 c'}{\partial x'^2} + \frac{\partial^2 c'}{\partial y'^2}\right) \quad \Rightarrow \frac{\partial c'}{\partial \tau} = \frac{1}{\tau_D}\left(\frac{\partial^2 c'}{\partial x'^2} + \frac{\partial^2 c'}{\partial y'^2}\right) \tag{58}$$

$$0 = \frac{\partial}{\partial x'}\left(c'\frac{\partial \phi'}{\partial x'}\right) + \frac{\partial}{\partial y'}\left(c'\frac{\partial \phi'}{\partial y'}\right) \tag{59}$$

$$At\ x' = 0\ and\ 1,\ \ \frac{\partial c'}{\partial x'} = 0, \quad c'\frac{\partial \phi'}{\partial x'} = 0 \tag{60}$$

$$\begin{aligned} At\ y' = s'(x',t),\ \ \frac{\partial c'}{\partial x'}n_x' + \frac{\partial c'}{\partial y'}n_y' &= \frac{i_{BV}L_x}{2FDc_0} - \frac{c'\left(\frac{M_W}{\rho}\frac{i_{BV}}{F}\right)L_x}{D} \\ &= -\frac{i_0 L_x}{2FDc_0}c'^{0.5}(0-\phi') + \frac{c'\left(\frac{M_W}{\rho}\frac{i_0}{F}\right)L_x}{D}c'^{0.5}(0-\phi') \\ &= -Da\cdot c'^{0.5}(0-\phi') + Pe\cdot c'^{1.5}(0-\phi') \\ c'\frac{\partial \phi'}{\partial x'}n_x' + c'\frac{\partial \phi'}{\partial y'}n_y' &= \frac{i_{BV}L_x}{2FDc_0} = -Da\cdot c'^{0.5}(0-\phi') \end{aligned} \tag{61}$$

$$\begin{aligned} At\ y = H,\ \ \frac{\partial c'}{\partial y'} &= \frac{i_{app,1C}CrateL_x}{2FDc_0} = \delta\ , \\ c'\frac{\partial \phi'}{\partial y'} &= \frac{i_{app,1C}CrateL_xF}{2FDc_0RT}\left(\frac{RT}{F}\right) = \delta \end{aligned} \tag{62}$$

$$At\ \tau = 0,\ \ c'(x',y',0) = 1,\ \ s'(x',0) = 0.1e^{-50(x'-0.5)^2} \tag{63}$$

$$\frac{\partial s'}{\partial \tau} = -\frac{M_w}{\rho}\frac{i_0}{F}\frac{3600}{L_x|Crate|}c'^{0.5}(0-\phi') = -\frac{Pe}{\tau_D}c'^{0.5}(0-\phi') \tag{64}$$

Model 2: Numerical Methodology

Model 2 can be solved using the same numerical approach as described in detail for

Model 1 in the previous section. The deforming domain can be fixed in space which will be followed by appropriate spatial and time discretization schemes. Figure 5 is a pictorial representation of the proposed hybrid numerical scheme used in this work to capture the evolving two-dimensional growth of the lithium deposition at the lithium anode surface. To facilitate the development of the numerical solution for Model 2, the transformed equations for Model 2 are listed below:

$$\frac{\left(\begin{array}{l} 2C\frac{\partial S}{\partial X}(H-S)(Y-H)\left(\frac{\partial \Phi}{\partial XY}\right)+C\left((H-Y)^2\left(\frac{\partial S}{\partial X}\right)^2+H^2\right)\left(\frac{\partial^2 \Phi}{\partial Y^2}\right) \\ +C(H-S)^2\left(\frac{\partial \Phi}{\partial X^2}\right)+\left((Y-H)^2\left(\frac{\partial S}{\partial X}\right)^2+H^2\right)\left(\frac{\partial C}{\partial Y}\right) \\ +(Y-H)\left(\left(\frac{\partial S}{\partial X}\right)(H-S)\left(\frac{\partial C}{\partial X}\right)+C\left((H-S)\left(\frac{\partial^2 S}{\partial X^2}\right)+2\left(\frac{\partial S}{\partial X}\right)^2\right)\right) \end{array}\right)}{(H-S)^2}=0 \quad [65]$$

$$\frac{\left(\begin{array}{l} (H-S)\left(\frac{\partial C}{\partial \tau}\right) \\ +(Y-H)\left(\frac{\partial S}{\partial \tau}\right)\left(\frac{\partial C}{\partial Y}\right) \end{array}\right)}{H-S}=\frac{1}{\tau_D}\frac{\left(\begin{array}{l} 2\left(\frac{\partial S}{\partial X}\right)(H-S)(Y-H)\left(\frac{\partial^2 C}{\partial XY}\right) \\ +\left((Y-H)^2\left(\frac{\partial S}{\partial X}\right)^2+H^2\right)\left(\frac{\partial^2 C}{\partial Y^2}\right) \\ +\left(\frac{\partial^2 C}{\partial X^2}\right)(H-S)^2 \\ +\left(\frac{\partial C}{\partial Y}\right)\left(\begin{array}{l} (H-S)\left(\frac{\partial^2 S}{\partial X^2}\right) \\ +2\left(\frac{\partial S}{\partial X}\right)^2 \end{array}\right)(Y-H) \end{array}\right)}{(H-S)^2\,Crate} \quad [66]$$

$$\frac{\partial C}{\partial Y}=\delta(1-S/H) \quad at \quad Y=1 \quad [67]$$

$$\frac{\partial \Phi}{\partial Y}=\delta(1-S/H) \quad at \quad Y=1 \quad [68]$$

$$\left(\frac{\partial C}{\partial X}-\frac{(H-Y)\frac{\partial S}{\partial X}\frac{\partial C}{\partial Y}}{H-S}\right)\left(\frac{\partial S}{\partial X}\right)-\frac{H\frac{\partial C}{\partial Y}}{H-S}=-Da\cdot C^{0.5}(-\Phi)\left(1+\left(\frac{\partial S}{\partial X}\right)^2\right)^{0.5} + Pe\cdot C^{1.5}(-\Phi)\left(1+\left(\frac{\partial S}{\partial X}\right)^2\right)^{0.5} \quad [69]$$

$$\left(\frac{\partial\Phi}{\partial X}-\frac{(H-Y)\frac{\partial S}{\partial X}\frac{\partial\Phi}{\partial Y}}{H-S}\right)\left(\frac{\partial S}{\partial X}\right)-\frac{H}{H-S}\frac{\partial C}{\partial Y}=-\frac{Da\cdot(-\Phi)\left(1+\left(\frac{\partial S}{\partial X}\right)^2\right)^{0.5}}{C^{0.5}} \quad [70]$$

$$\frac{\partial S}{\partial \tau}=-\frac{Pe}{\tau_D}(-\Phi)(C)^{0.5} \quad [71]$$

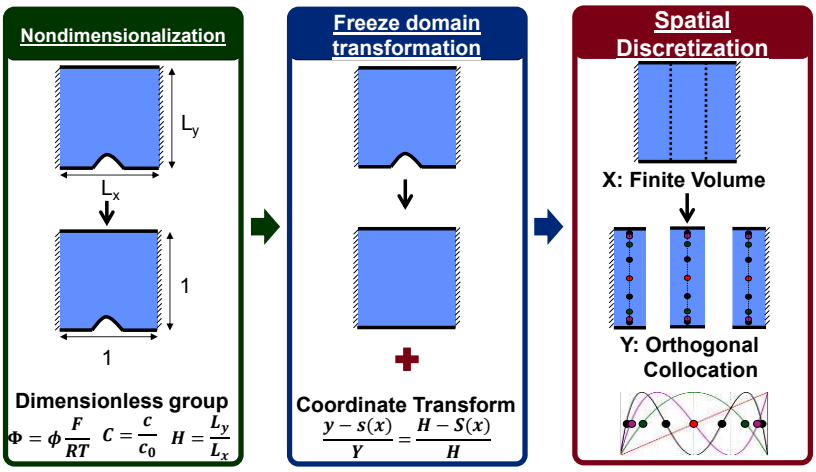

Figure 5. Schematic representing the proposed novel hybrid approach.

The numerical results obtained for liquid phase concentration and potential are presented and discussed in the next section both Models 1 and 2 along with some validations of the proposed numerical scheme with those obtained using the finite-element method. Before completing this section, we want to mention that the spatial discretization equations described for Model 1 are based on 2nd order expressions for the ease of discussion and representation. The actual results shown in the next section were obtained using the cell-centered 4th order finite difference discretization schemes in X which are included in Table II for reference. The scaled equations can be discretized using higher order schemes for improving the numerical accuracy as desired. Note that since the Gaussian seed is reasonably smooth, 4th order finite difference approximation was used. For semicircular seeds, because of singularity, 2nd order finite difference was sufficient at the first cycle. As the deposit grows, if the boundary becomes smoother, 4th order finite difference approximation can be used.

Table II. 4th order discretization schemes

U* = *C*, *Φ* or *S	
$U_{-1}(\tau)$	$=-\frac{54}{23}U_1(\tau)+\frac{104}{23}U_2(\tau)-\frac{27}{23}U_3(\tau)$
$U_0(\tau)$	$=\frac{21}{23}U_1(\tau)+\frac{3}{23}U_2(\tau)-\frac{1}{23}U_3(\tau)$
$U_{N+1}(\tau)$	$=-\frac{1}{23}U_{N-2}(\tau)+\frac{3}{23}U_{N-1}(\tau)+\frac{21}{23}U_N(\tau)$
$U_{N+2}(\tau)$	$=-\frac{27}{23}U_{N-2}(\tau)+\frac{104}{23}U_{N-1}(\tau)-\frac{54}{23}U_N(\tau)$

Results and Discussion

The numerical simulations were performed to solve the moving boundary models using the in-house codes in Maple for the hybrid numerical scheme which agreed well with the results obtained from the ALE approach implemented with finite element methods using in-house codes as well as the commercial solver, COMSOL Multiphysics (Version 5.1). The domain of interest was simulated over multiple charge and discharge cycles in order to obtain the variation of concentration and potential with time and track the plating and stripping of the lithium metal at the anode surface.

Validation of Numerical Scheme

Figures 6(a-b) show the near-perfect agreement between ALE approach implemented by COMSOL Multiphysics and in-house codes for the evolution of moving boundary and the average potential at the anode/electrolyte moving interface in Model 1. Figure 6(c) highlights the importance of the appropriate selection of the in-built moving boundary parameters in the commercial solvers that might sometimes drastically reverse the trends in results.

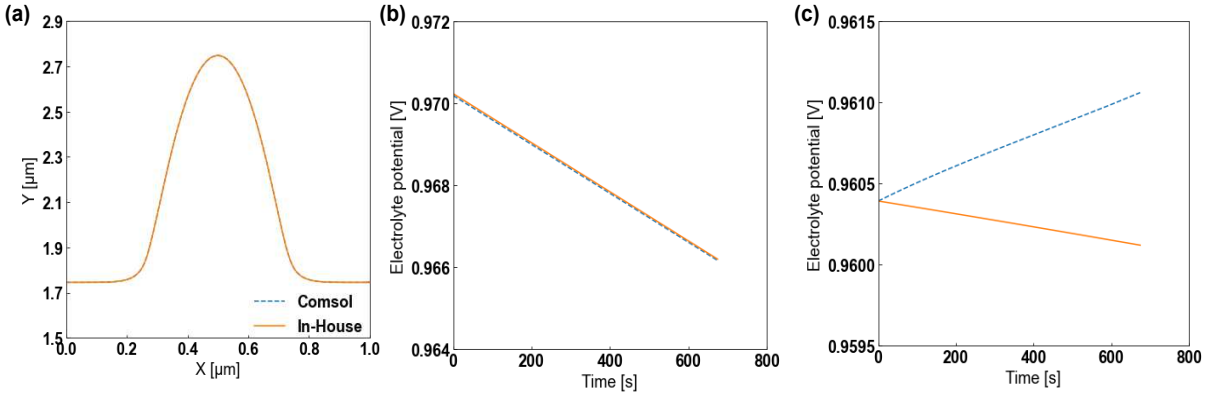

Figure 6. Comparison for the results obtained using COMSOL Multiphysics and in-house codes for (a) moving boundary evolution, (b) average potential at the cathode/electrolyte interface, and (c) average potential at the anode/electrolyte interface using in-built smoothing settings.

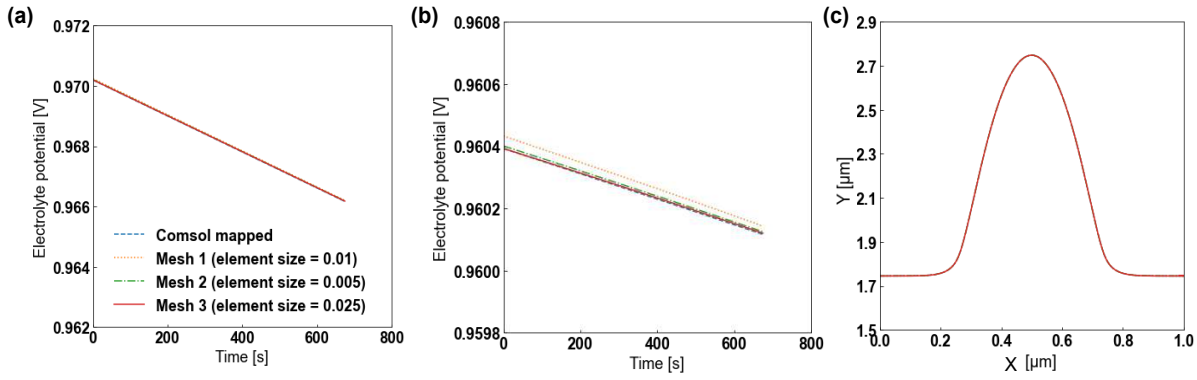

Figure 7. Comparison of in-house FEM codes with COMSOL Multiphysics for Model 1.

Figure 7 shows the comparison between the in-house codes for the finite element based ALE approach with those obtained from COMSOL Multiphysics for Model 1. The values are compared at the tip of the seed at anode and the corresponding center point at the cathode for electrolyte potential. These plots also include the results for the mesh and time step independence for the present simulations. A fine mesh size of 0.0025 and time step of 1 were found to be adequate for the present simulations.

Electrolyte Concentration and Potential Profiles.

The solutions for the liquid phase concentration and potential in Model 2 are plotted in Fig. 8 at the tip of the seed deposit ($X = 0.5$) and the base at anode surface ($X = 0$) for one cycle of charge followed by discharge. The characteristic inverse signature in concentration during plating can be seen to be captured well with the present Model 2. Over several cycles at uniform rates for charge and discharge at 1C, the mass of the lithium ions in the domain remains conserved but the variation in the electrolyte concentration results in irreversible signatures at the lithium anode due to the growth of the seed deposit over cycles as discussed in the following section.

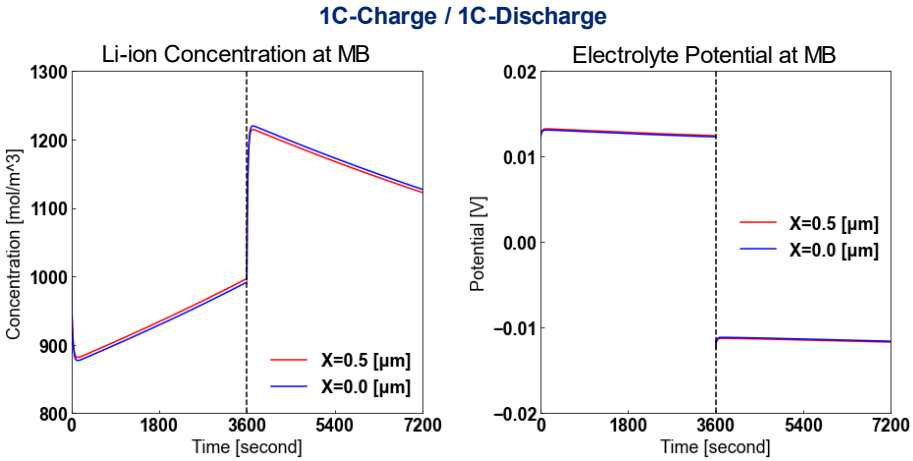

Figure 8. Electrolyte concentration and potential profiles for 1C charge/1C discharge for 1 cycle using Model 2.

Evolution of Moving Surface

The evolution of the moving surface with charging and discharging of the battery is plotted in Fig. 9 for Model 1 over 20 cycles. The initial morphology is conserved after each cycle owing to the Laplacian model for electrolyte potential in the absence of concentration gradients.

With Model 2, as shown in Fig. 10, for the first cycle, the plating/stripping of the lithium metal with charging/discharging alters the seed geometry negligibly and the moving Gaussian surface is observed to reattain the initial shape at the end of the Cycle 1 (Fig. 10a). As the battery is cycled continuously to reach 20 cycles (Fig. 10b), the final seed geometry is seen to have a higher growth at the tip as compared to the base (anode surface) which might be responsible for a dendritic growth at the site of initial deposit over cycles.

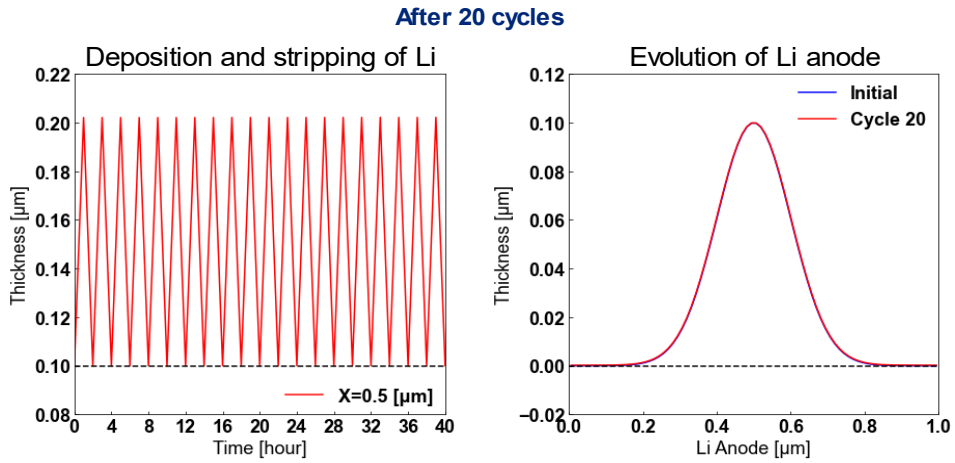

Figure 9. Variation in the moving surface for 1C charge/1C discharge over 20 cycles using Model 1.

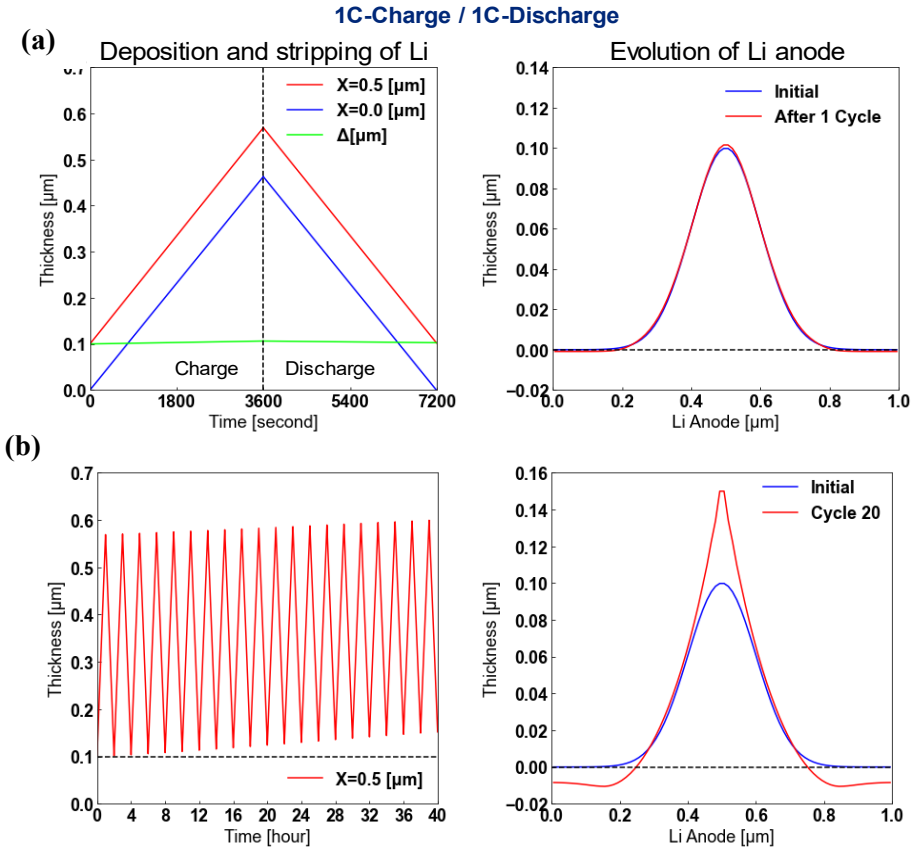

Figure 10. Evolution of moving surface at the tip of the seed over 20 cycles depicting deposition/stripping of the lithium metal using Model 2.

Effect of Charge/Discharge Rates

The variation in the rates for charge and discharge is also responsible for promoting the growth of the seed with time over multiple charge/discharge cycles as shown for the test case of 0.1C (charging) followed by 0.33C (discharging) in Fig. 11.

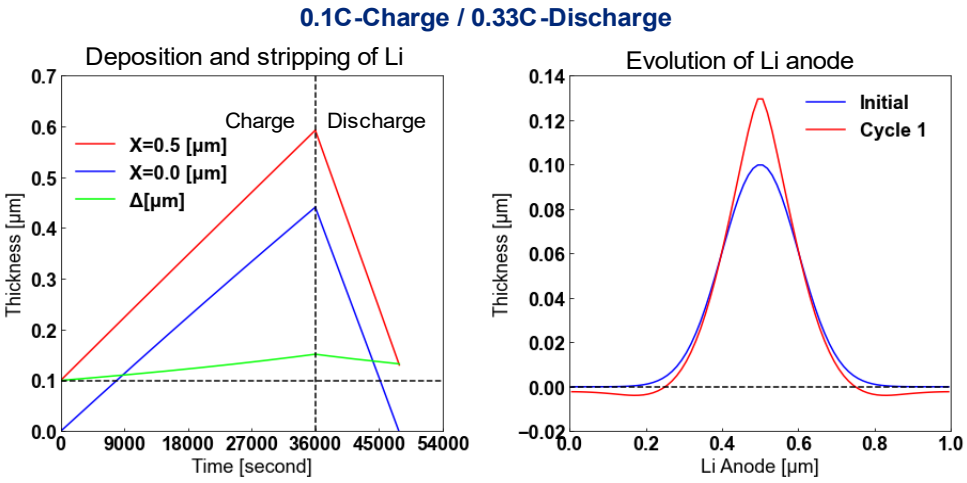

Figure 11. Evolution of moving surface at the tip of the seed.

A higher discharge rate can be responsible for a higher growth as compared to our base case with 1C charge/ 1C discharge rates. Similarly, we can expect to have a deduction in the growth profile for a certain cycling protocol. This can be further investigated as a separate optimization study to arrive at a charging protocol which inhibits the growth of the deposits. Table III enlists the values for geometric and cell parameters used in the present simulations for the results shown in this section.

Table III. Baseline model parameters used in the simulations

Symbol	Parameter	Values	Units
Geometrical Parameters			
L_x	Domain length in x	10e-6	m
L_y	Domain length in y	50e-6	m
Operational parameters			
$i_{app,1C}$	Applied current density	10	A/m^2
i_0	Exchange current density	20	A/m^2
c_0	Initial electrolyte concentration	1000	mol/m^3
T	Operating temperature	298	K
Material parameters			
D	Diffusion coefficient	1e-11	m^2/s
M_W	Molar mass of Lithium	6.941	g/mol
ρ	Density of Lithium	0.534	g/cm^3
General parameters			
R	Universal Gas Constant	8.314	J/molK
F	Faraday's Constant	96487	C/mol

Conclusions

A robust and efficient 2D model and efficient code have been developed for the multiscale modeling of the morphological evolution of lithium in lithium metal batteries.

This model has been specifically tailored to encompass electrochemical models, kinetics, and microstructure evolution. We have been able to obtain higher order of accuracy with less memory footprint. The simulations are also fast as compared to conventional algorithms, and we have been able to simulate up to 100 cycles of charge/discharge in the presented lithium metal battery within a few minutes of simulation time. The future steps include further development of these models leading to improved performance for the lithium batteries. This model can also help understand the effect of design, transport, and kinetic parameters on the deposition profile of the lithium metal and serve as a platform to develop an optimized charging protocol for lithium metal batteries.

The models are available as executable codes, soon to be hosted at the corresponding author's website (http:/sites.utexas.edu/maple) after the submission of full manuscript.

Acknowledgments

The authors would like to thank the U.S. Department of Energy (DOE) for providing partial financial support for this work, through the Advanced Battery Material Research (BMR) Program (Battery 500 Consortium) and the Texas Materials Institute for partial monetary support of this work. This paper describes objective technical results and analysis. Any subjective views or opinions that might be expressed in the paper do not necessarily represent the views of the U.S. Department of Energy or the United States Government. Supported by the Laboratory Directed Research and Development program at Sandia National Laboratories, a multimission laboratory managed and operated by National Technology and Engineering Solutions of Sandia, LLC., a wholly owned subsidiary of Honeywell International, Inc., for the U.S. Department of Energy's National Nuclear Security Administration under contract DE-NA-0003525.

References

1. C. Monroe and J. Newman, *J. Electrochem. Soc*., **150**, A1377 (2003).
2. V. Srinivasan, K. Higa, P. Barai, and Y. Xie, in *Handbook of Materials Modeling*. W. Andreoni and S. Yip, Editors, p. 1193, Springer, Cham (2020).
3. A. J. Sanchez, E. Kazyak, Y. Chen, K. H. Chen, E. R. Pattison, and N. P. Dasgupta, *ACS Energy Lett.*, **5**(3), 994 (2020).
4. F. Hao, A. Verma, and P. P. Mukherjee, *ACS Appl. Mater. Inter*., **10**, 26320 (2018).
5. G. Li and C. W. Monroe, *Annu. Rev. Chem. Biomol. Eng*., **11**, 277 (2020).
6. R. Alkire, T. Bergh, and R. L. Sani, *J. Electrochem. Soc*., **125**, 1981 (1978).
7. J. L. Barton and J. O. Bockris, *Proc. R. Soc. Lond. A*, **268**, 485 (1962).
8. J. N. Chazalviel, *Phys. Rev. A*, **42**, 7355 (1990).
9. K. N. Wood, E. Kazyak, A. F. Chadwick, K. H. Chen, J. G. Zhang, K. Thornton, and N. P. Dasgupta, *ACS Cent. Sci.*, **2**, 790 (2016).
10. A. Ferrese and J. Newman, *J. Electrochem. Soc*., **161**, A948 (2014).
11. J. Liu, Z. Bao, Y. Cui, E. Dufek, J. B. Goodenough, P. Khalifah, Q. Li, B. Liaw, P. Liu, A. Manthiram, Y.S. Meng, V. R. Subramanian, M. F. Toney, V. V. Viswanathan, M. S. Whittingham, J. Xiao, W. Xu, J.Yang, X. Yang, and J. Zhang, *Nat. Nanotechnol.,* **14**, 180 (2019).

12. P. Bai, J. Li, F. R. Brushett, and M. Z. Bazant, *Energy Environ. Sci*., **9**, 3221 (2016).
13. A. Pei, G. Zheng, F. Shi, Y. Li, and Y. Cui., *Nano Lett*., **17**(2), 1132 (2017).
14. X. Zhang, Q. J. Wang, K. L. Harrison, K. Jungjohann, B. L. Boyce, S. A. Roberts, P. M. Attia, and S. J. Harris, *J. Electrochem. Soc*., **166**, A3639 (2019).
15. Z. Hong and V. Viswanathan, *ACS Energy Lett*., **3**, 1737 (2018).
16. K. Shah, A. Subramaniam, L. Mishra, T. Jang, M. Z. Bazant, R. D. Braatz, and V. R. Subramanian, *J. Electrochem. Soc*., **167**, 133501 (2020).
17. A. Mistry, C. Fear, R. Carter, C. T. Love, and P. P. Mukherjee, *ACS Energy Lett*., **4**, 156 (2019).
18. L. Gao and Z. Guo, *Comput. Mater. Sci*., **183**, 109919 (2020).
19. R. Akolkar, *J. Power Sources*, **232**, 23 (2013).
20. Z. Hong and V. Viswanathan, *ACS Energy Lett*., **3**(7), 1737 (2018)
21. S. Sripad, D. Korff, S. C. DeCaluwe, and V. Viswanathan, *J. Chem. Phys*., **153**(19), 194701 (2020).
22. X. Zhang, Q. J. Wang, K. L. Harrison, S. A. Roberts, and S. J. Harris, *Cell Rep. Phys. Sci*., **1**, 100012 (2020).
23. T. Jang, L. Mishra, K. Shah, P. Mittal, A. Subramaniam, M. P. Gururajan, S. A. Roberts, and V. R. Subramanian, *ECS Meet. Abstr*., **MA2021-01** 985 (2021).
24. A. Subramaniam, J. Chen, T. Jang, N. R. Geise, R. M. Kasse, M. F. Toney, and V. R. Subramanian, *J. Electrochem. Soc*., **166**, A3806 (2019).
25. M. Uppaluri, A. Subramaniam, L. Mishra, V. Viswanathan, and V. R. Subramanian, *J. Electrochem. Soc*., **167**, 160547 (2020).
26. J. Newman and K. E. Thomas-Alyea, *Electrochemical Systems,* 3rd ed., John Wiley & Sons, Inc., Hoboken, NJ, (2004).
27. H. G. Landau, *Q. Appl. Math*., **8**, 81 (1950).
28. S. K. Godunov, *Math. Sbornik*, **47**, 271 (1959).
29. W. M. Deen, *Analysis of Transport Phenomena*, 2nd ed., Oxford University Press, Inc., New York, NY, (2012).